**ARL**

**US Army Research Laboratory**

# Computational Investigation of a Pitch-Oscillating Canard on Lift Enhancement and Tip Vortex Mitigation

**by Joseph D Vasile**

**US Army Research Laboratory**

# Computational Investigation of a Pitch-Oscillating Canard on Lift Enhancement and Tip Vortex Mitigation

**by Joseph D Vasile**
*Weapons and Materials Research Directorate, ARL*

| REPORT DOCUMENTATION PAGE | | *Form Approved*<br>*OMB No. 0704-0188* |
|---|---|---|

| 1. REPORT DATE *(DD-MM-YYYY)* | 2. REPORT TYPE | 3. DATES COVERED (From - To) |
|---|---|---|
| April 2017 | Technical Report | March–December 2016 |

| 4. TITLE AND SUBTITLE | 5a. CONTRACT NUMBER |
|---|---|
| Computational Investigation of a Pitch-Oscillating Canard on Lift Enhancement and Tip Vortex Mitigation | |
| | 5b. GRANT NUMBER |
| | 5c. PROGRAM ELEMENT NUMBER |

| 6. AUTHOR(S) | 5d. PROJECT NUMBER |
|---|---|
| Joseph D Vasile | AH43 |
| | 5e. TASK NUMBER |
| | 5f. WORK UNIT NUMBER |

| 7. PERFORMING ORGANIZATION NAME(S) AND ADDRESS(ES) | 8. PERFORMING ORGANIZATION REPORT NUMBER |
|---|---|
| US Army Research Laboratory<br>ATTN: RDRL-WML-E<br>Aberdeen Proving Ground, MD 21005-5066 | ARL-TR-7995 |

| 9. SPONSORING/MONITORING AGENCY NAME(S) AND ADDRESS(ES) | 10. SPONSOR/MONITOR'S ACRONYM(S) |
|---|---|
| | 11. SPONSOR/MONITOR'S REPORT NUMBER(S) |

**12. DISTRIBUTION/AVAILABILITY STATEMENT**

Approved for public release; distribution is unlimited.

**13. SUPPLEMENTARY NOTES**

**14. ABSTRACT**

A 2-D National Advisory Committee for Aeronautics (NACA) 0012 airfoil and 3-D NACA 0015 canard undergoing a dynamic ramp pitch-oscillating motion were investigated computationally. The effect of amplitude and reduced frequency on augmenting lift for both configurations was considered. The study showed lift enhancement for both configurations at $M_\infty = 0.5$ and $M_\infty = 0.2$ for all amplitudes and reduced frequencies at angles of attack poststall. Furthermore, the effect of the dynamic motion on the development of the tip vortex was explored. The time-averaged flow solution for the pitch-oscillating canard revealed lower vorticity magnitude and less coherence of the tip vortex downstream. For the parameters investigated, increasing the amplitude of the oscillation proved to be the most effective in enhancing lift as well as reducing the strength of the tip vortex. The encouraging results indicate that further research in unsteady aerodynamics to increase the control authority of canard-controlled projectiles is necessary.

**15. SUBJECT TERMS**

CFD, dynamic stall, tip vortex, enhanced canard control, lift augmentation

| 16. SECURITY CLASSIFICATION OF: | | | 17. LIMITATION OF ABSTRACT | 18. NUMBER OF PAGES | 19a. NAME OF RESPONSIBLE PERSON |
|---|---|---|---|---|---|
| | | | | | Joseph D Vasile |
| a. REPORT | b. ABSTRACT | c. THIS PAGE | UU | 42 | 19b. TELEPHONE NUMBER (Include area code) |
| Unclassified | Unclassified | Unclassified | | | 410-306-1794 |

# Contents

## List of Figures

## List of Tables

## Acknowledgments

## 1. Introduction

Current aerodynamic research for guided munitions has primarily been focused on improving the maneuverability of projectiles to perform at a wider range of engagement and operating conditions.[1–6] Moreover, these efforts focus on increasing the control authority while concurrently reducing adverse wake effects from movable lifting surfaces.[7–9] Extensive research has shown significant control authority detriment due to the flow interactions between the downwash of trailing-edge vortices from control surfaces impacting the tail fins downstream.[10–19] To address these issues, the US Army Research Laboratory (ARL) is investigating techniques that can increase maneuverability by both augmenting lift and mitigating the vortex-fin flow interactions. Viable techniques will expand the capabilities of guided projectiles, through increased accuracy and precision, against both stationary and moving targets.

One area of research that has demonstrated a significant increase in lift for airfoils has been unsteady aerodynamics.[20–22] Specifically, the benefit of oscillatory pitching and plunging airfoils have been extensively studied.[23–29] This dynamic motion can result in higher lift as well as delay the onset of stall. The unsteady lift augmentation is the product of an airfoil undergoing rapid change in angle of attack, which causes a leading-edge vortex to be produced and then shed downstream along the suction side of the airfoil. The vortex increases suction pressure as it rolls downstream, temporarily increasing lift. This periodic lift augmentation is generally referred to as dynamic stall.[30–33] A comprehensive collection of studies have examined dynamic stall and its application. However, to the best of the author's knowledge, none have studied the viability of using dynamic stall for increased performance of canard-controlled projectiles. Furthermore, very little work has been performed investigating the effect of dynamic stall on the development of the tip vortex. The majority of these studies focus on either 2-D vortex street[34–36] (i.e., spanwise rollers) or rotorcraft applications, specifically studying the interaction of rotor blades of a helicopter impacting vortices shed by preceding rotor blades (i.e., blade-vortex interactions).[37–40]

The purpose of the present study is to determine if unsteady pitch-oscillating canards could be a viable solution to increase the control authority of guided projectiles. The effect of a pitch-oscillating canard for lift augmentation and its effectiveness in reducing the strength of the tip vortex to reduce adverse flow interactions downstream is investigated. The computational study is split into 2 investigations. First, lift augmentation for an unsteady 2-D airfoil at $M_\infty = 0.5$ is

considered. Second, both lift enhancement and tip vortex mitigation of an unsteady 3-D canard at $M_\infty = 0.2$ and $0.5$ are investigated. In both studies, the effect of reduced frequency and amplitude of the oscillation on dynamic stall was an area of interest.

## 2.    Technical Approach

The computational investigation is split as follows: 1) a 2-D airfoil (National Advisory Committee for Aeronautics [NACA] 0012) study to reduce the number of parameters (i.e., reduced frequency and amplitude) for the prescribed ramp-oscillation that enhances lift at $M_\infty = 0.5$ and 2) a 3-D rectangular planform canard (NACA 0015 cross-sectional airfoil) associated with typical dimensions used for canard-controlled projectiles at $M_\infty = 0.5$ and $0.2$. In addition to assessing lift augmentation, the effect of the dynamic motion on the development of the tip vortex was investigated.

A ramp-oscillation motion was prescribed for each computational case (see Section 3.1). The dynamic ramp motion increases the angle of attack of the lifting surface linearly while superimposing a high-frequency oscillation about the quarter-chord of the airfoil. The mathematical relationship of the rotation of the lifting surface with respect to the freestream velocity, about the quarter-chord, as a function of time, is described in Eq. 1.

$$\alpha(t) = \omega_1 t + A \cdot sin(\omega_2 t), \tag{1}$$

where $\alpha(t)$ is the angle of attack as a function of time, $t$, $\omega_1$, and $\omega_2$ are the rate and frequency of the linear ramp and oscillation, respectively, and $A$ is the amplitude of the oscillation. This dynamic motion was chosen in order to model a practical command for canard-controlled projectiles. Furthermore, the dynamic motion was selected to exploit the full dynamic motion effect as found in previous unsteady aerodynamic studies,[20–33] namely the superposition of rapidly increasing angle of attack to delay stall (ramp) and periodic lift augmentation due to classic dynamic stall (oscillation). Through the combination of these 2 mechanisms, it was hypothesized that the same dynamic effect could be achieved with less amplitude of oscillation in both augmenting lift as well as delaying stall. The rate and frequency of the dynamic motion was selected based on a reduced frequency value, $k$. As defined in most studies on unsteady aerodynamics, the reduced frequency is mathematically expressed in Eq. 2.

$$k_j = \frac{\omega_j c}{2 U_\infty} \bigg|_{j=1,2}, \tag{2}$$

where $c$ is the chord length of the airfoil, $U_\infty$ is the freestream velocity, and $j$ denotes either the linear ramp rate, 1, or oscillation frequency, 2. For the present study, the reduced frequency of the linear ramp rate was held constant at $k_1 = 0.005$. This value was selected based on reference values of usual actuator driven canard-controlled rate (e.g., 5–13 Hz). Note that the dynamic stall effect of enhancing lift is not expected to originate from the linear ramp motion due to the relatively low reduced frequency value. The dynamic stall effect is dependent on the reduced frequency of the oscillation and is most noticeable when the value is greater than 0.05. The reduced frequency for oscillatory motion was studied at $k_2 = 0.5$ and 1.0. Furthermore, 4 amplitudes, A = 0°, 0.5°, 1.5°, and 5°, were investigated for the 2-D case, whereas 3 amplitudes, A = 0°, 1.5°, and 5°, were studied for the 3-D case. For both computational cases, the linear ramp motion (i.e., pitch oscillation set to zero amplitude [A = 0°]), was selected for the baseline case. Table 1 summarizes the test matrix for both computational cases.

**Table 1    Computational test matrix**

| Case | $M_\infty$ | $k_1$ | $k_2$ | A (°) |
|---|---|---|---|---|
| 2-D airfoil (NACA 0012) | 0.5 | 0.005 | 0.5, 1.0 | 0, 0.5, 1.5, 5 |
| 3-D canard (NACA 0015) | 0.2, 0.5 | 0.005 | 0.5, 1.0 | 0, 1.5, 5 |

## 2.1  Geometries and Computational Domains

### 2.1.1  Two-Dimensional Airfoil

The 2-D airfoil used for the initial simulations, shown in Fig. 1, has a chord length, $c = 1$ m, with a cross-sectional profile of a NACA 0012 airfoil. The computational domain was meshed with GAMBIT v2.4 from ANSYS Fluent, a C-grid mesh containing approximately 55,000 cells, and has an approximate radial distance of 5 chord lengths from the leading edge of the airfoil to the domain surfaces. The first cell spacing was set to $4 \times 10^{-6}$ m to ensure $y^+$ values were at or below 1.0 along the surface of the airfoil for accurate boundary layer prediction.
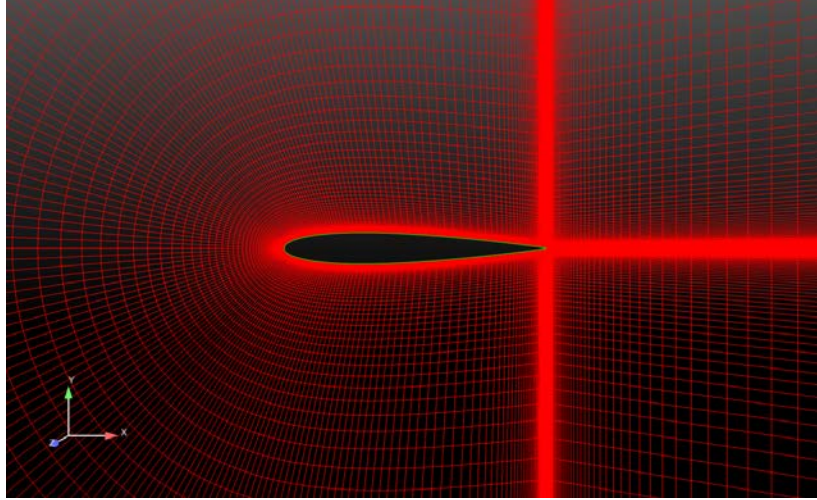
**Fig. 1     Two-dimensional airfoil geometry with mesh**

### 2.1.2   Three-Dimensional Canard

The 3-D canard model, shown in Fig. 2, is an unswept, finite canard with a chord length, $c = 0.021$ m, a semi-span, $b/2 = 0.063$ m, and a cross-sectional NACA 0015 airfoil profile. The computational domain was meshed with MIME from Metacomp Technologies.[41] The rectangular domain spans an approximately 48 chord lengths equidistant in both streamwise and normal directions from the leading edge of the canard. The width of the domain is approximately 22 chord lengths from the root of the canard to the outboard domain surface. A mesh density cylinder was used to refine the mesh in the region near the canard tip and wake region to resolve the tip vortex. The origin of the density box was aligned to the canard tip, with a radius of approximately 2 chord lengths, spanning approximately 10 chord lengths downstream (Fig. 2b). The total mesh size was approximately 33 M cells, consisting of triangular surface cells, with prism layers used along the surface and tetrahedral cells for the rest of the domain. The first cell wall spacing of the prism layers was set to $2 \times 10^{-6}$ m to ensure $y^+$ values of less than 1 along the surface of the canard.
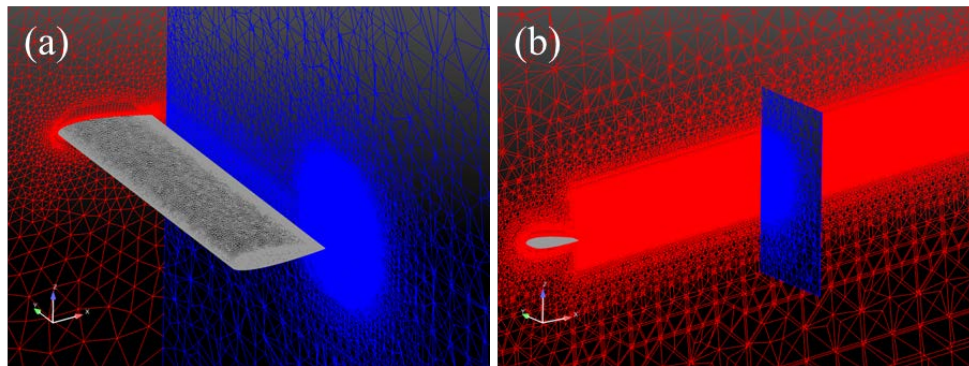


**Fig. 2     Three-dimensional canard and computational domain**

## 2.2  Computational Fluid Dynamics (CFD) Solution Technique

The commercially available code, CFD++ v15.1.1 by Metacomp Technologies, Inc.,[42] was used for all simulations. The 2-D or 3-D compressible Reynolds-averaged Navier-Stokes (RANS) equations were numerically solved to compute the flow solution for each respective case. Both steady-state and transient simulations were employed.

Simulations were performed on the Cray XC40 (Excalibur) and Cray XC30 (Lightning) supercomputers located at ARL's Department of Defense Supercomputing Resource Center (DSRC) at Aberdeen Proving Ground, Maryland, and US Air Force Research Laboratory DSRC at Wright-Patterson Air Force Base, Ohio, respectively.

For all steady-state simulations, the solution was advanced toward convergence using a point-implicit time-integration scheme with local time-stepping defined by the Courant-Friedrichs-Lewy (CFL) number. A linear ramping schedule was used to gradually increase the CFL number from 1 to 50 over the first 100 iterations, after which the CFL remained constant until convergence was reached. The multigrid W-cycle method with a maximum of 4 cycles and a maximum of 20 grid levels were used to accelerate convergence. Implicit temporal smoothing was applied for the increased stability, which is especially useful where strong transients arise. The spatial discretization function was a second-order, upwind scheme using a Harten-Lax-van Leer-Contact Riemann solver and Metacomp's multi-dimensional Total-Variation-Diminishing flux limiter. Convergence for the total forces and moments was typically achieved in a few thousand iterations, with residuals reducing at 5 orders or more in magnitude.

For all transient RANS simulations, the dual-time step method was employed with the point-implicit time-integration scheme using a global time step and an inner time step. For the transient planar pitching simulations, the global time step of the transient simulation was selected based on 100 steps per cycle of pitch-oscillation with 20 inner iterations per global time step. The number of global time steps were selected based on the time it took the dynamic ramp schedule to reach an angle of attack of approximately 25°.

For the 2-D simulation, a realizable k-$\varepsilon$ 2-equation turbulence model was used, whereas for the 3-D simulation, Menter's k-$\omega$ Shear Stress Transport 2-equation model was used. For the current study, initialization of the turbulence transport was completed by setting the turbulence intensity to 3% and the turbulent-to-molecular viscosity ratio to 50, as the length scale was not known. The choice of turbulence model may be an important factor in numerical modeling of the tip vortex and will need to be further investigated.

## 2.3  Flowfield and Boundary Conditions

All computations were completed using a free-stream temperature and pressure of 288.15 K and 101,325 Pa, respectively. The study was conducted at $M_\infty = 0.5$ (170 m/s) and 0.2 (68 m/s). The wind-axis coordinate system was used such that streamwise velocity, U, is positive downstream; cross-stream velocity, V, is positive toward the sidewall (inboard direction); and normal velocity, W, is positive upward. The free-stream velocity and chord length of the geometries were used to nondimensionalize important parameters and coordinates, denoted by an asterisk (*). The domain was initialized using free-stream conditions everywhere. The far-field boundary was set as "characteristic-based" inflow/outflow. This boundary condition takes the specified free-stream conditions and solves a Riemann problem at the boundary using the supplied data as a virtual state outside the domain. The surfaces of the airfoil and canard were modeled as adiabatic, no-slip, viscous walls with solve-to-wall methodology. The sidewall for the 3-D domain was modeled as an inviscid slip wall. For the transient simulations, the dynamic motion was prescribed through a file-based single-axis rotation, which allowed for the entire grid to rotate as a function of time.

## 3.  Results and Discussion

### 3.1  Two-Dimensional Airfoil

The 2-D NACA 0012 airfoil case was first investigated to determine if the dynamic stall effect could be achieved from the prescribed dynamic ramp motion at $M_\infty = 0.5$. The dynamic ramp schedule of the airfoil at 2 reduced frequencies ($k_2 = 0.5$ and 1.0) and 4 amplitudes (A = 0.0, 0.5, 1.5, and 5.0) is presented in Figs. 3a and 3b, respectively. The dynamic ramp schedule is the combination of a linear ramp superimposed with a high-frequency oscillation. For this study, the linear rate is held constant, while the oscillation frequency was varied. The high-frequency oscillation begins when the angle of attack of the airfoil is $\alpha = 5°$. This angle was selected to ensure that the airfoil never experiences a negative angle of attack during the ramp schedule. The baseline case is denoted by the dashed black line.
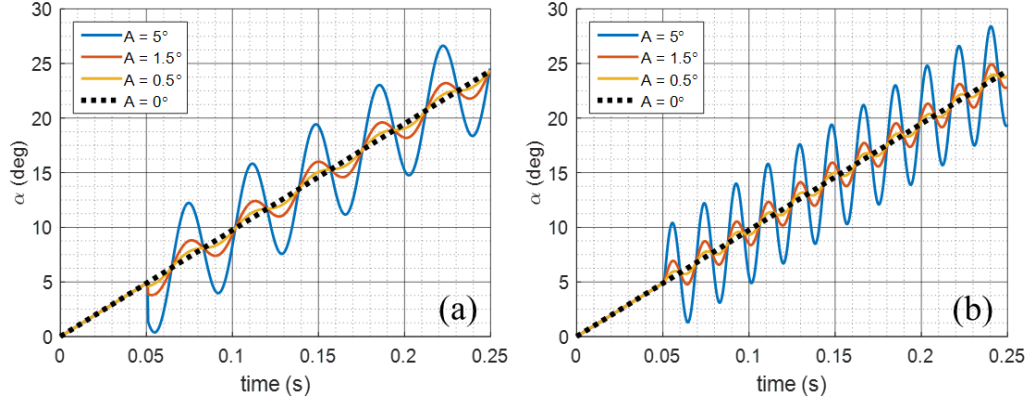
**Fig. 3**    Prescribed dynamic ramp motion for the 2-D airfoil at $k_2 = 0.5$ (a) and 1.0 (b)

The sectional lift coefficient, $C_L$, of the airfoil was computed in CFD++ for all parameter combinations. The equation for the section lift coefficient for the 2-D airfoil case is presented in Eq. 3.

$$C_L = \frac{L}{\frac{1}{2}\rho_\infty U_\infty^2 c} ,$$

(3)

where $L$ is the lift force, $\rho_\infty$ and $U_\infty$ are the free-stream density and velocity, respectively, and $c$ is the chord length of the airfoil. To compare the lift values between the actuated (i.e., oscillatory) cases with the baseline for a given angle of attack, the lift coefficient was plotted against the equivalent mean angle of attack (i.e., baseline angle of attack). The lift coefficient as a function of angle of attack for the baseline (black dashed line) and the dynamic motion cases is presented in Fig. 4. The baseline case shows the typical linear increase of lift with increasing angle of attack until approximately $\alpha = 9°$. At this angle the flow begins to separate from the upper surface of the airfoil, which causes the lift curve to become nonlinear. At $\alpha = 14°$, the airfoil stalls, characterized by a peak followed by a precipitous drop in lift. Further increase in angle of the attack results in unsteady, nonlinear lift along with a large increase in drag. For the investigated configuration, the lift coefficient oscillates since the airfoil is pitch oscillating about the mean angle of attack (Figs. 4a and 4c). The period of the oscillation is correlated to the reduced frequency of the prescribed dynamic motion. For all amplitudes, the lower reduced frequency, $k_2 = 0.5$, exhibits a longer period as well as larger fluctuations in lift than the higher reduced frequency, $k_2 = 1.0$, case. The larger the amplitude of oscillation, the larger the fluctuation in lift. For both cases, the lift fluctuation remains sinusoidal about the mean angle of attack until approximately $\alpha = 9°$, when the peaks of the lift curve become deformed. The lift fluctuation behaves sinusoidal longer for the lower reduced frequency case than the higher-frequency case. These fluctuations in lift continue with increase in angle of attack.
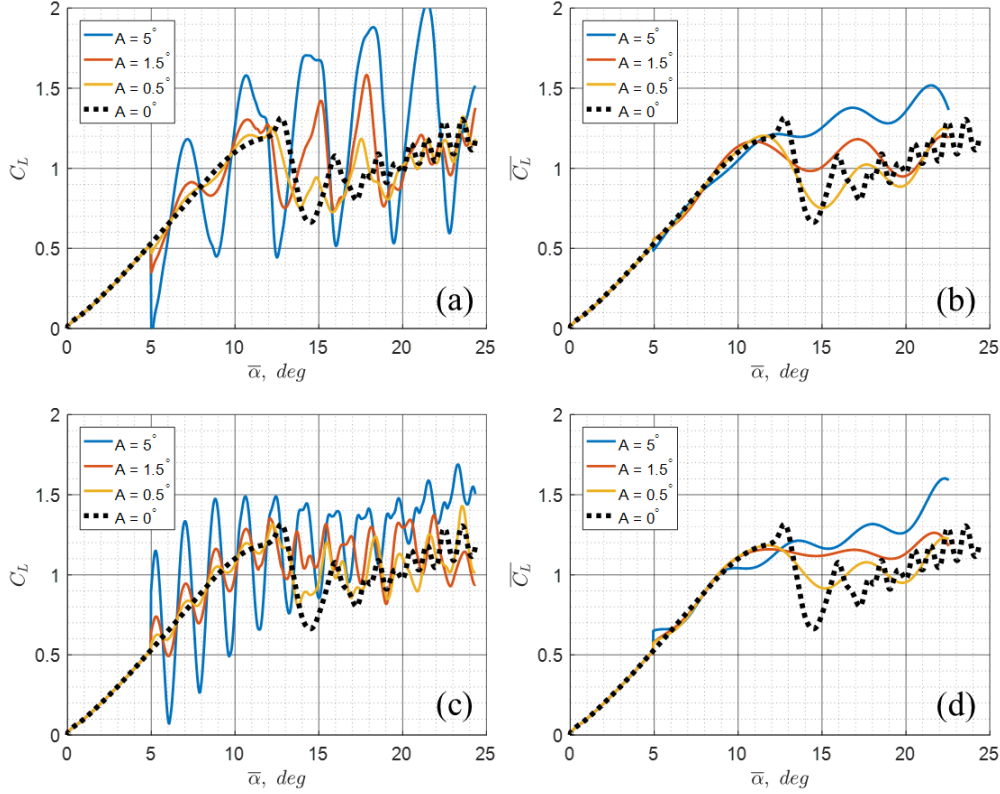
**Fig. 4    Lift coefficient of dynamic airfoil as a function of equivalent mean angle of attack, unfiltered (a, c) and filtered (b, d), for reduced frequency of oscillation of $k_2 = 0.5$ (a–b) and 1.0 (c–d), $M_\infty = 0.5$**

The large fluctuations in lift make it difficult to distinguish the full effect of the dynamic motion in enhancing lift; therefore, the lift data for both cases was filtered and is presented in Figs. 4b and 4d. The lift curves for the actuated cases were filtered using a low pass filter to remove the oscillation due to the dynamic motion. A fast Fourier transform algorithm was used to analyze the frequency components of the lift curve and to perform the filter. From the filtered data for both reduced frequencies, the smallest amplitude case, $A = 0.5°$, seems to have little to no effect on enhancing the lift of the airfoil, whereas the largest amplitude case, $A = 5°$, shows considerable lift enhancement at higher angles of attack compared with the baseline. Furthermore, the $A = 1.5°$ and $5°$ cases do not exhibit the precipitous drop in lift at $\alpha = 14°$, therefore indicating that stall was successfully delayed. The results from the 2-D case suggest that lift augmentation is possible using a dynamic motion. The favorable results from the 2-D case warranted further exploration of the dynamic motion effect for 3-D configurations.

## 3.2 Three-Dimensional Canard

The 3-D canard (NACA 0015 airfoil) case was studied to investigate the dynamic stall effect on a more-realistic control surface with dimensions that are typical of canard-controlled projectiles. The favorable results from the 2-D case were used to help determine the computational test matrix. Following the same procedure as the 2-D case, a prescribed ramp-oscillation dynamic motion was simulated for the 3-D canard case.

### 3.2.1 Unsteady Lift Enhancement

Similar to the 2-D airfoil case (Fig. 3), the dynamic ramp schedule of the 3-D canard is a linear ramp superimposed with high-frequency oscillation beginning when the angle of attack of the airfoil equals $\alpha = 5°$. Two reduced frequencies ($k_2 = 0.5$ and $1.0$) at 3 amplitudes ($A = 0.0$, $1.5$, and $5.0$) were simulated at 2 free-stream Mach numbers, $M_\infty = 0.5$ and $0.2$. The lift coefficient for the 3-D canard case was computed similarly to the 2-D case (Eq. 3) and is mathematically expressed in Eq. 4.

$$C_L = \frac{L}{\frac{1}{2}\rho_\infty U_\infty^2 S} \,, \tag{4}$$

where $S$ is the planform area of the canard (i.e., $S = c \cdot b/2$). The lift coefficient as a function of angle of attack for the baseline (black dashed line) and the dynamic motion cases at $M_\infty = 0.5$ and $0.2$ are presented in Fig. 5 and Fig. 6, respectively. Similar to the 2-D case, the baseline lift distribution for the 3-D case increases linearly until $\alpha = 10°$ then nonlinearly until reaching a peak at approximately $\alpha = 14°$ (Fig. 5). Note that the peak value of lift is less than the peak achieved for the 2-D airfoil case. The reduction in lift is due to the downwash generated by the tip vortex. Furthermore, there is a less-pronounced drop in lift after stall. The unfiltered data (Fig. 5a and 5c) shows fluctuations in lift at both reduced frequencies and increasing fluctuations with increasing amplitude of oscillation.

Following the same procedure as the 2-D case, the lift coefficient data was filtered to remove the frequency associated with the prescribed oscillation frequency. The filtered data (Fig. 5b and 5d) show that the dynamic motion is ineffective in increasing lift at small angles of attack but is able to increase lift past the stall angle, thus delaying the onset of stall. Although the data have been filtered, there is still an oscillation of lift present at higher angles of attack, suggesting that the inherent nonlinear behavior of poststall is still present for the actuated cases. The results indicate that the amplitude of the oscillation is a more-sensitive parameter for lift enhancement than the effect of reduced frequency of the oscillation. The augmentation of lift is more noticeable for the larger amplitude. The results suggest

that the higher reduced frequency, $k_2 = 1.0$, for $A = 1.5°$, is more effective in enhancing lift than the lower reduced frequency (Fig. 5d). Moreover, the effect of reduced frequency is less noticeable for the higher amplitude, $A = 5°$. The results suggest that unsteady lift enhancement is possible for canard-controlled projectiles. However, achieving high-amplitude (e.g., $>1.5°$) oscillations at the given reduced frequency could prove to be impractical.
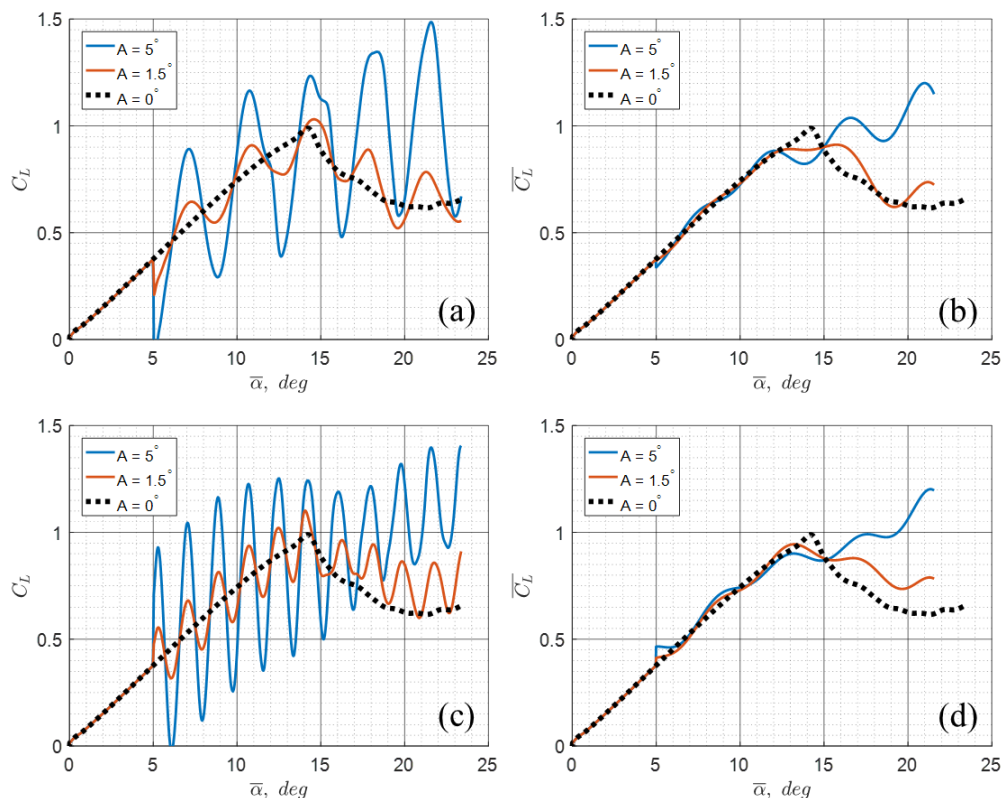


**Fig. 5    Lift coefficient of dynamic canard as a function of equivalent mean angle of attack, unfiltered (a, c) and filtered (b, d), for reduced frequency of oscillation of $k_2 = 0.5$ (a–b) and 1.0 (c–d), $M_\infty = 0.5$**

The lift coefficient as a function of equivalent mean angle of attack for all parameter combinations at $M_\infty = 0.2$ is presented in Fig. 6. Compared with that of the higher-speed case, $M_\infty = 0.5$, the baseline lift distribution for the $M_\infty = 0.2$ case increases linearly until $\alpha = 14°$ then nonlinearly until reaching a peak at approximately $\alpha = 19°$ (Fig. 6). The lower-speed case stalls at a larger angle than the higher-speed case at the same reduced frequency, $k_1 = 0.005$, while undergoing linear ramp motion. For the actuated cases, similar behavior to that of the higher-speed case is exhibited; the unfiltered data show large oscillation in lift for the canard that is magnified while undergoing prescribed large amplitude oscillation (i.e., $A = 5°$). The lift coefficient distribution increases proportionally to the prescribed dynamic motion at lower angles of attack. However, it seems to exhibit nonlinear behavior poststall.

Furthermore, the lower reduced frequency causes the canard to achieve larger lift values poststall than the higher reduced frequency at the same amplitude (Fig. 6a). As described previously, the lift coefficient data were filtered to remove the frequency associated with the prescribed oscillation and are presented in Figs. 6b and 6d. As was observed for the higher-speed case, the dynamic motion is ineffective in increasing lift at small angles of attack. However, it is able to delay the onset of stall. For all cases, the larger amplitude, A = 5°, is more effective in augmenting lift at higher angles of attack.
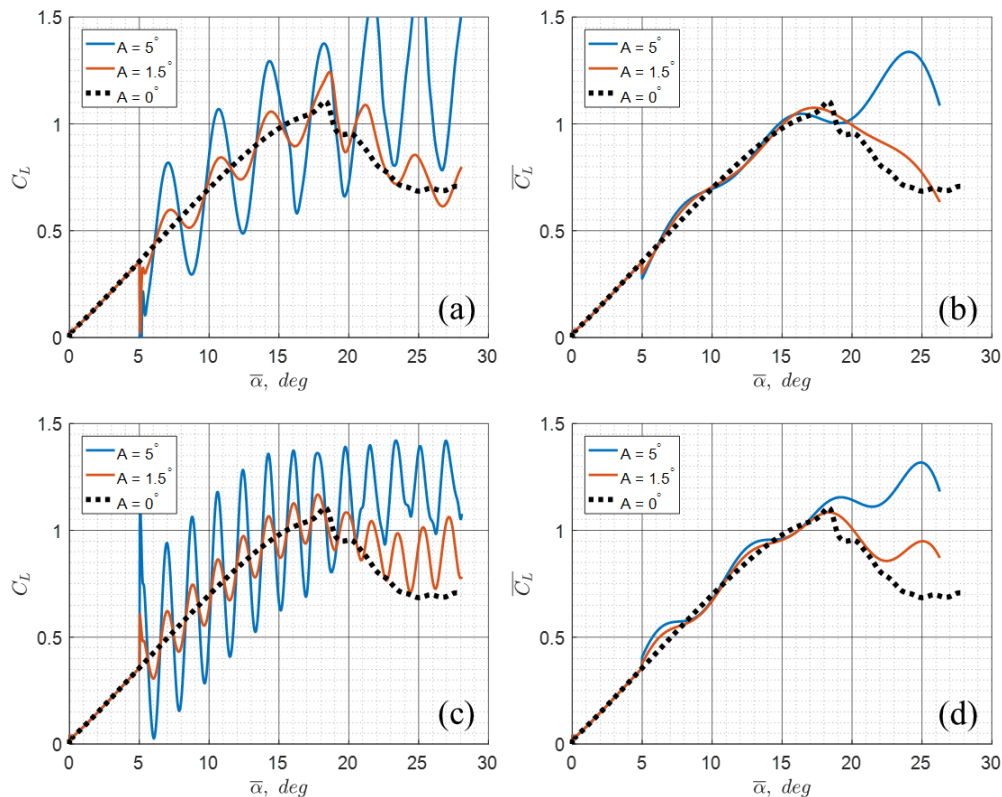


**Fig. 6     Lift coefficient of dynamic canard as a function of equivalent mean angle of attack, unfiltered (a, c) and filtered (b, d), for reduced frequency of oscillation of $k_2$ = 0.5 (a–b) and 1.0 (c–d), $M_\infty$ = 0.2**

The influence of the tip vortex is evident through the reduction in peak lift coefficient of the 3-D case compared with the peak achieved for the 2-D case. The vortex strength increases with angle of attack, creating downwash that effectively reduces lift while increasing drag of the canard. In addition to the lift detriment, the tip vortex trails downstream, affecting the performance of control surfaces in the wake of the canard. Therefore, it is of high interest to investigate the effect of dynamic motion on the tip vortex.

11

### 3.2.2 Tip Vortex Mitigation

The effect of pitch oscillation on the development of the tip vortex was simulated using a modified ramp-oscillation motion. Similar to the previous prescribed motion, this motion superimposes a high-frequency oscillation on a linear ramp. However, unlike the previous prescribed motion, the modified motion performs the high-frequency oscillation when the canard reaches $\alpha = 10°$. Furthermore, when the oscillation begins, the motion is held at a mean value of $\alpha = 10°$, which results in a motion in which pitch oscillates about $\alpha = 10°$. The prescribed dynamic ramp schedule for the baseline (A = 0°) and actuated cases (A = 1.5° and 5°) at a reduced frequency of $k_2 = 1.0$, at $M_\infty = 0.5$, is presented in Fig. 7. This modified dynamic motion is mathematically expressed in Eq. 5.

$$\alpha(t) = \begin{cases} \omega_1 t & \text{if } \alpha \leq 10° \\ A\sin(\omega_2 t) + 10° & \text{if } \alpha > 10° \end{cases}. \tag{5}$$
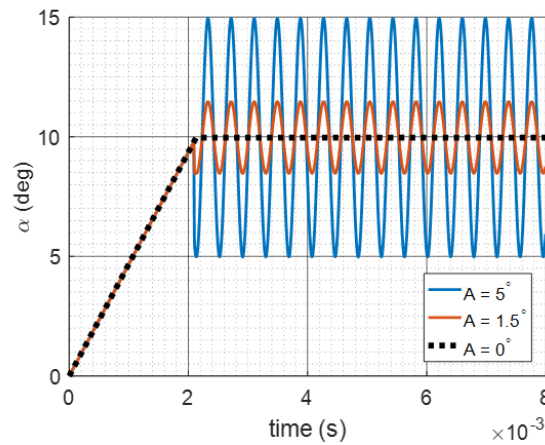


**Fig. 7** **Prescribed dynamic motion of 3-D canard for tip vortex mitigation at $k_2$ = 1.0, $M_\infty$ = 0.5**

The tip vortex was qualitatively assessed using contour slices of the domain near the canard tip. A plane of nondimensional vorticity magnitude for all combinations near the canard tip (y/c = 0.1, or 2 mm, inboard from the tip) at $M_\infty = 0.5$ undergoing pitch oscillation about $\alpha = 10°$ at $k_2 = 0.5$ and 1.0 is presented in the following videos, Figs. 8–11.
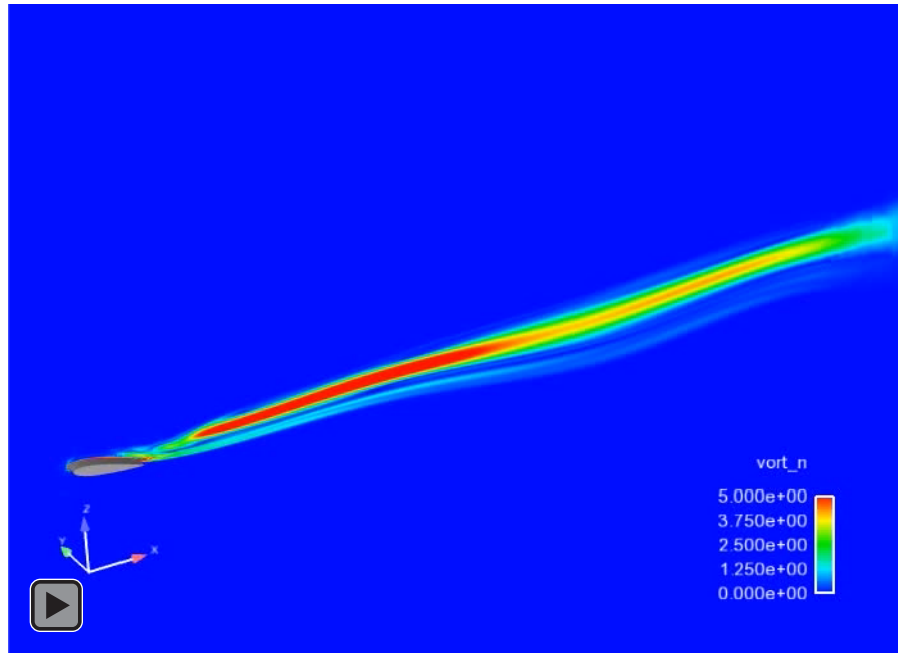
**Fig. 8** **Contour of time-accurate nondimensional vorticity magnitude near canard tip (y/c = 0.1 inboard from tip) undergoing pitch-oscillation about α = 10° at an amplitude of A = 1.5° and reduced frequency k₂ = 0.5 at M∞ = 0.5**
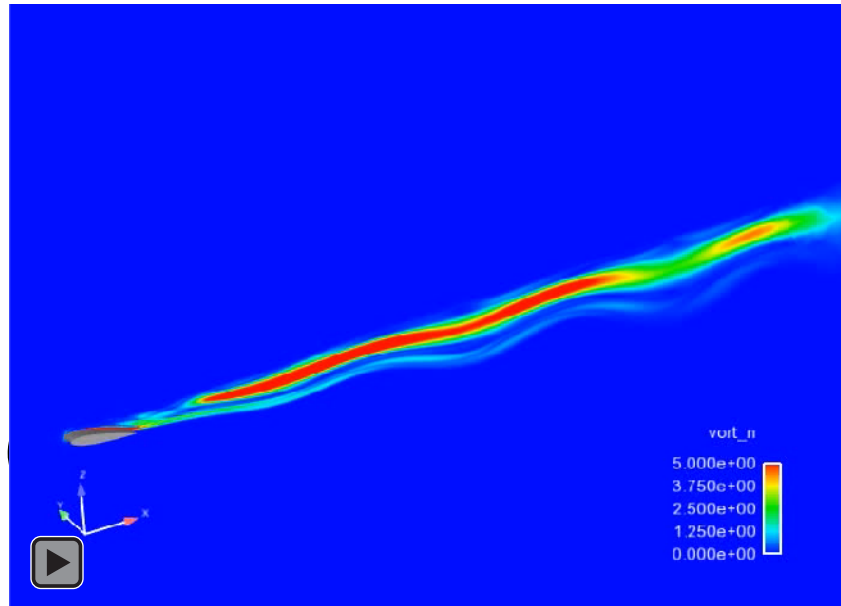


**Fig. 9** **Contour of time-accurate nondimensional vorticity magnitude near canard tip (y/c = 0.1 inboard from tip) undergoing pitch-oscillation about α = 10° at an amplitude of A = 1.5° and reduced frequency k₂ = 1.0 at M∞ = 0.5**
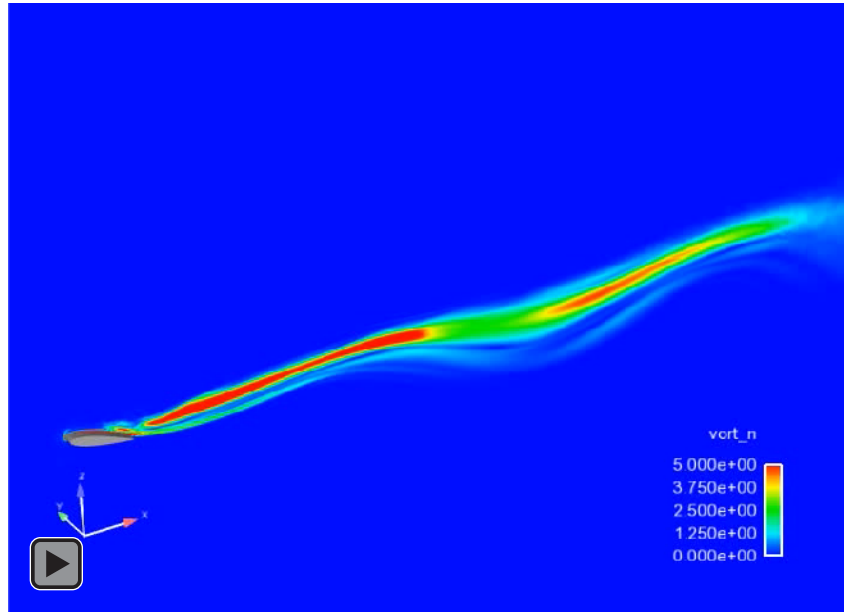
**Fig. 10  Contour of time-accurate nondimensional vorticity magnitude near canard tip (y/c = 0.1 inboard from tip) undergoing pitch-oscillation about α = 10° at an amplitude of A = 5.0° and reduced frequency k₂ = 0.5 at M∞ = 0.5**
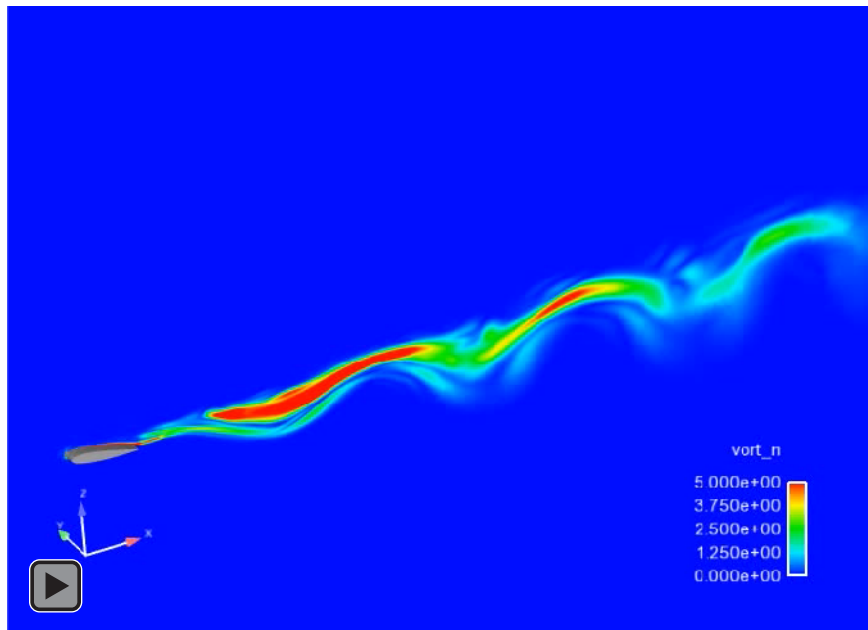


**Fig. 11  Contour of time-accurate nondimensional vorticity magnitude near canard tip (y/c = 0.1 inboard from tip) undergoing pitch-oscillation about α = 10° at an amplitude of A = 5.0° and reduced frequency k₂ = 1.0 at M∞ = 0.5**

Clearly, the development of the tip vortex is affected due to actuation. The pitch-oscillation causes an oscillation in vorticity concentration downstream. To fully analyze and compare the development of the tip vortex, the flow solution was time-averaged over the last cycle of oscillation for all parameter combinations. A plane of nondimensional vorticity magnitude for all combinations near the canard tip (y/c = 0.1, or 2 mm, inboard from the tip) at M∞ = 0.5 and 0.2 is presented in

Figs. 12 and 13, respectively. The qualitative results indicate that the development of the tip vortex downstream for both speeds, $M_\infty = 0.5$ and 0.2, are almost identical.



**Fig. 12 Contour of time-averaged (over the last oscillation cycle) nondimensional vorticity magnitude near canard tip (y/c = 0.1 inboard from tip) for baseline (a), a = 1.5° (b, d) and A = 5° (c, e) at reduced frequencies k₂ = 0.5 (b–c) and 1.0 (d–e), M∞ = 0.5**

**Fig. 13    Contour of time-averaged (over the last oscillation cycle) nondimensional vorticity magnitude near canard tip (y/c = 0.1 inboard from tip) for baseline (a), a = 1.5° (b, d) and A = 5° (c, e) at reduced frequencies $k_2$ = 0.5 (b–c) and 1.0 (d–e), $M_\infty$ = 0.2**

The time-averaged vorticity magnitude for the baseline case at both speeds show the development of a vortex that trails far downstream (Figs 12a and 13a). The vortex is characterized by a concentration of increased vorticity magnitude, which remains coherent downstream. Farther downstream, the vorticity concentration diffuses due to viscosity. For all combinations, there is a clear reduction in vorticity magnitude when the canard undergoes dynamic motion. Because of the pitch oscillating motion, the vorticity magnitude is less, and the vortex is less coherent (Figs. 12b–e and 13b–e). The radial vorticity influence increases in size farther downstream most likely due to increased viscous diffusion. The larger amplitude of oscillation is more effective in reducing the magnitude but causes the vortex

16

influence to increase radially (Figs. 12c and 12e, and 13c and 13e). The effect of reduced frequency is evident in the shape of the wake flow from the canard. The vorticity magnitude concentration appears as a standing wave in which the nodes of the wave are associated with high concentrations of vorticity. Moreover, since the higher reduced frequency is twice the lower reduced frequency value, the wave length of the vorticity concentration wave of the higher reduced frequency is half the length of the lower reduced frequency actuated case.

In addition to vorticity magnitude, the turbulent kinetic energy (TKE) was investigated downstream of the canard tip. The development of a tip vortex is associated with an increase of the TKE due to 2 mechanisms: 1) the introduction of an unsteady coherent flow structure and 2) the random velocity fluctuations present in the mean shear flow of the tip vortex core. The normalized TKE (*TKE\**) is defined as

$$TKE^* = \frac{1}{2}\frac{(u'u'+v'v'+w'w')}{U_\infty^2}, \tag{6}$$

where *u', v',* and *w'* are the fluctuating components of velocity obtained from Reynolds decomposition of the velocity field. The time-averaged, nondimensional *TKE\** for all parameter combinations near the canard tip at $M_\infty = 0.5$ and 0.2 is presented in Figs. 14 and 15, respectively. As previously observed for vorticity magnitude, the TKE field for all combinations at both speeds, $M_\infty = 0.5$ and 0.2, are qualitative similar. The baseline case shows high concentration of TKE downstream of the canard tip due to the formation of the vortex. There is a higher concentration of TKE closer to the trailing edge for the higher speed; however, the region is larger radially for the lower speed. At the lower speed, the tip vortex exhibits more unsteadiness, evident by large regions of TKE farther downstream compared with the higher-speed case. Farther downstream, for both speeds, the TKE diffuses due to viscosity. The effect of actuation is shown through the distribution of the TKE concentration downstream. Similar to the vorticity field, the shape of the TKE region of the tip vortex is dependent on the actuation frequency. The results show that actuation causes TKE to diffuse sooner downstream compared with the baseline. Moreover, increasing the amplitude of actuation augments diffusion, which is shown to be more effective than increasing actuation frequency.
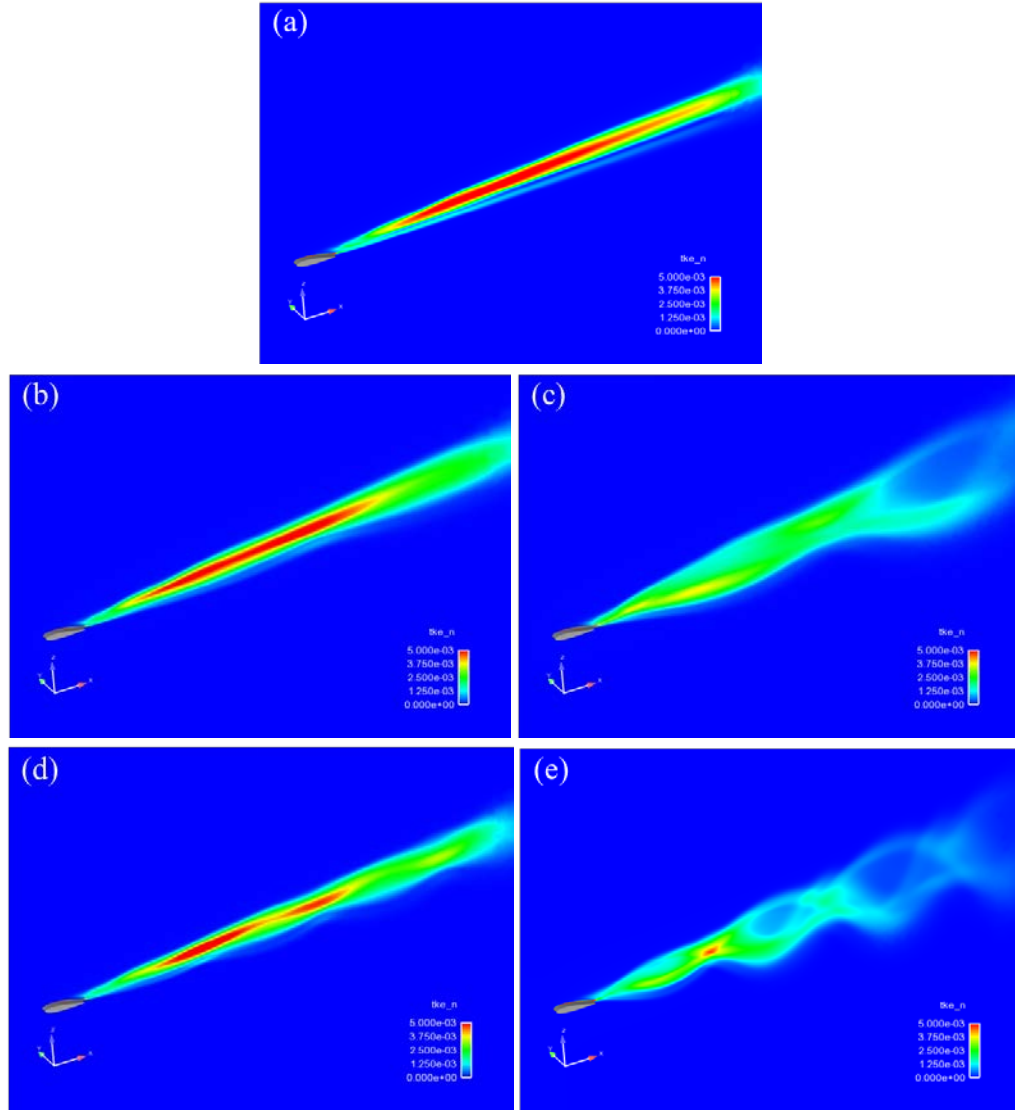
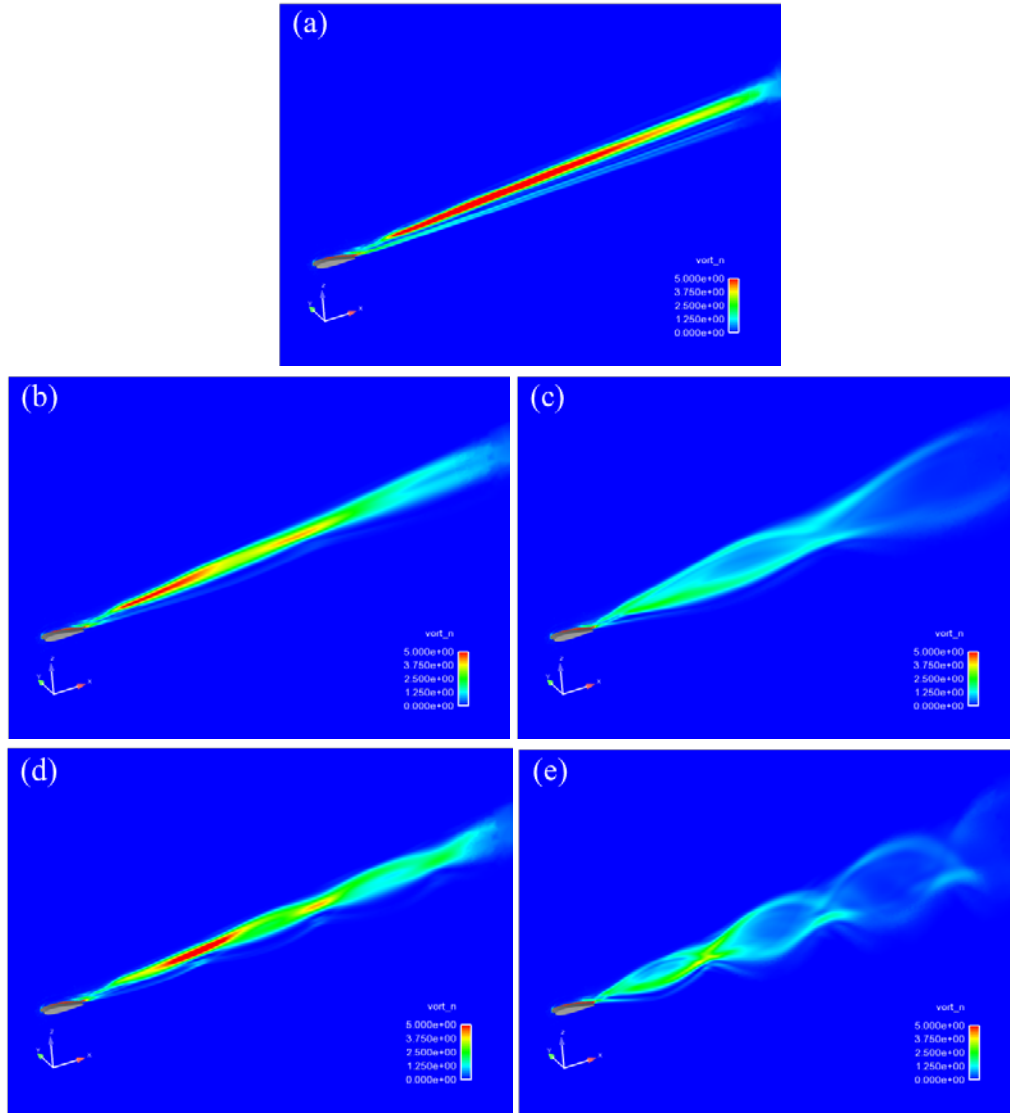**Fig. 14    Contour of time-averaged (over the last oscillation cycle) nondimensional TKE, near canard tip (y/c = 0.1 inboard from tip) for baseline (a), A = 1.5° (b, d) and A = 5° (c, e) at reduced frequencies $k_2$ = 0.5 (b–c) and 1.0 (d–e), $M_\infty$ = 0.5**

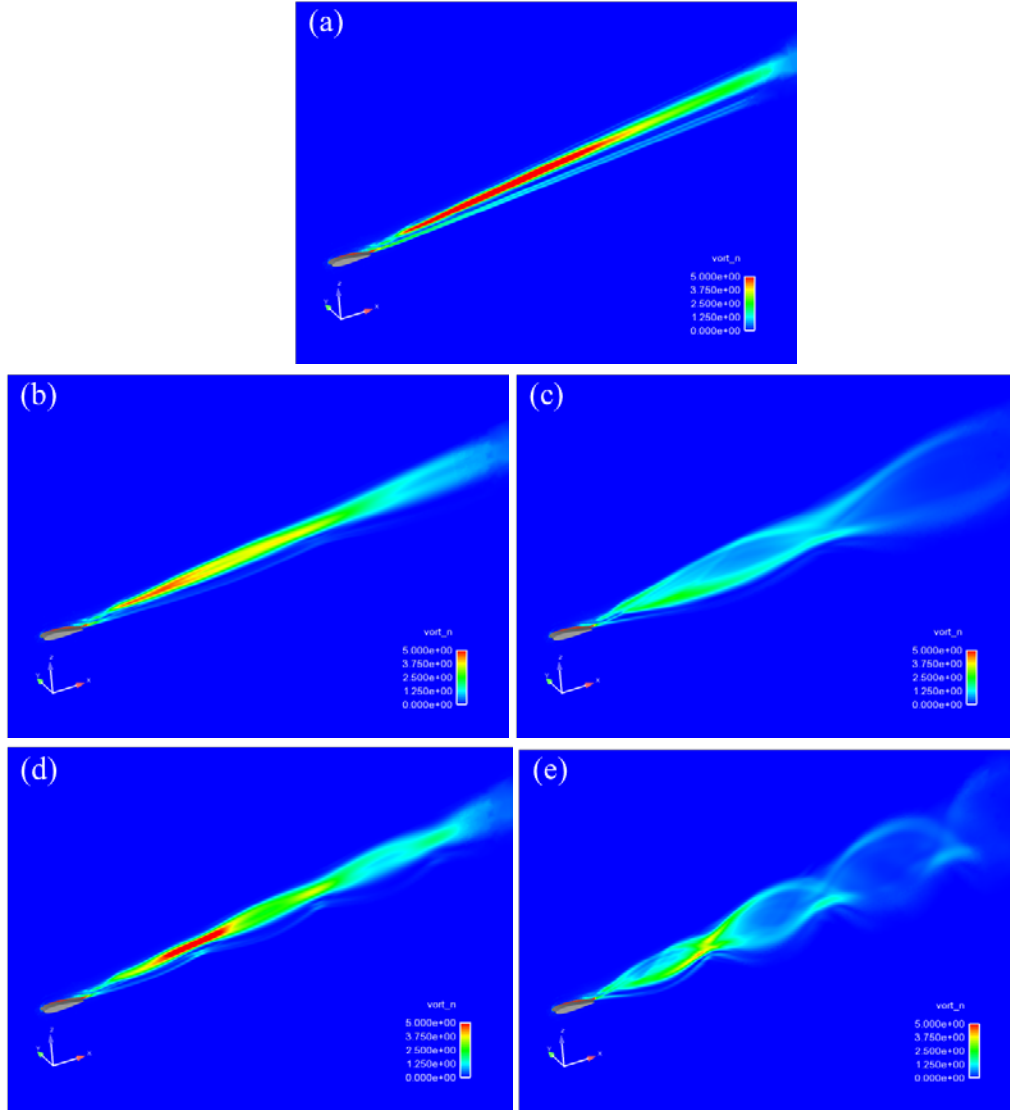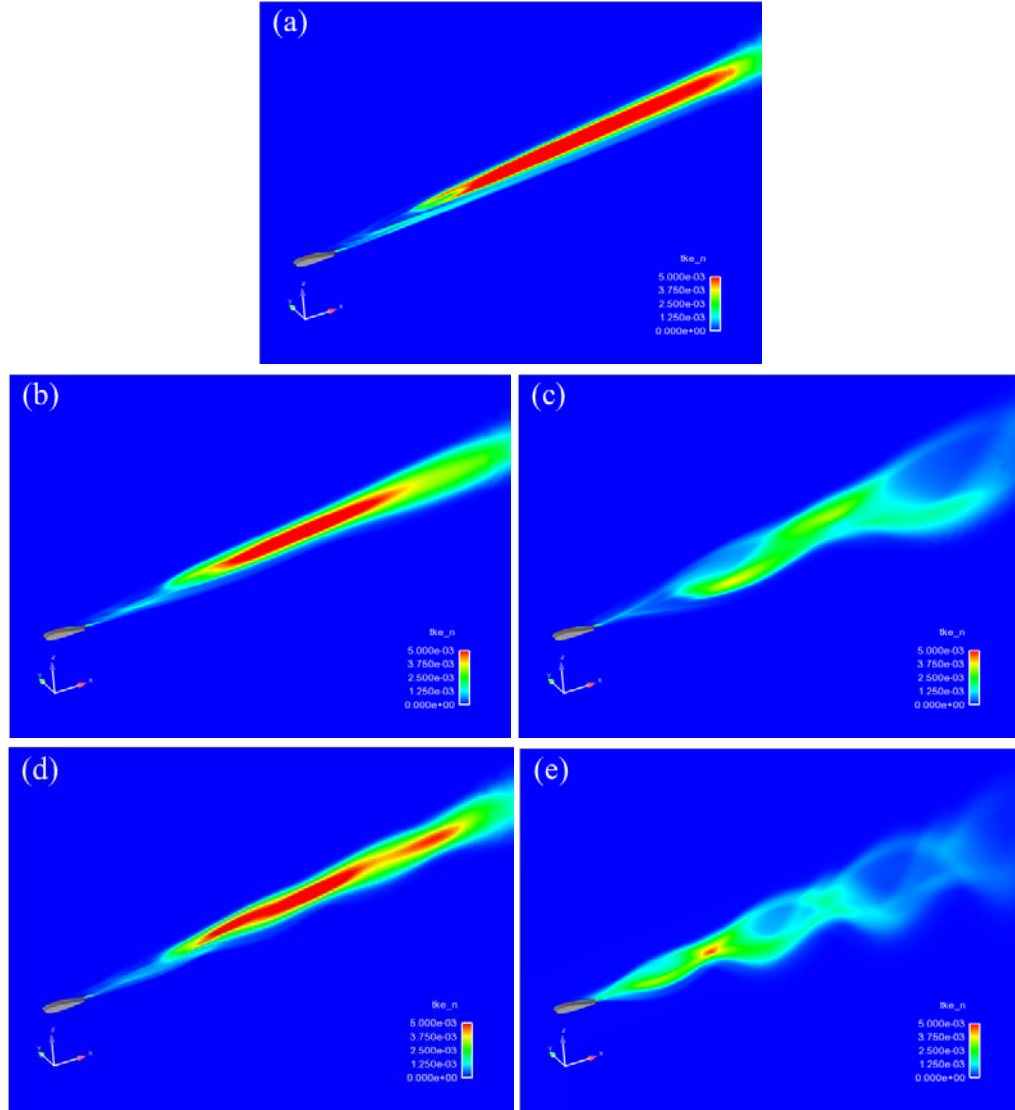**Fig. 15    Contour of time-averaged (over the last oscillation cycle) nondimensional TKE, near canard tip (y/c = 0.1 inboard from tip) for baseline (a), A = 1.5° (b, d) and A = 5° (c, e) at reduced frequencies $k_2$ = 0.5 (b–c) and 1.0 (d–e), $M_\infty$ = 0.2**

The time-averaged slices provide a qualitative assessment of the tip vortex; however, a more quantitative approach is necessary to fully understand the effect of the dynamic motion on the tip vortex wake flow. Since there was no observed qualitative difference between $M_\infty$ = 0.5 and 0.2 cases in the development of the tip vortex, only the $M_\infty$ = 0.5 case was further explored.

To quantify the tip vortex, contour slices were obtained downstream of the trailing edge tip of the canard. From the time-averaged flow solution, a total of 11 contour slices, ranging from x/c = 0 to x/c = 10, spaced evenly every x/c = 1, were studied. The effectiveness of pitch oscillation on mitigating the tip vortex was studied by

identifying and detecting vortices in the selected contour slices. Many techniques are available to characterize vortices in flows.[43–47] In the present case, 5 parameters were investigated: 1) peak vorticity magnitude, 2) Q-criterion, 3) circulation, 4) tangential velocity, and 5) vortex core radius. Vortices are often identified in flows by regions of high vorticity. However, high-vorticity regions are also present in parallel shear flows where no vortices are present. Therefore, the Q-criterion was developed to help define vortices in flows as spatial regions where the vorticity tensor dominates the rate of strain. The Q-criterion, Q, is mathematically expressed in Eq. 6.

$$Q = \frac{1}{2}(\|\boldsymbol{\Omega}^2\| - \|\boldsymbol{S}^2\|) > 0, \tag{6}$$

where $\boldsymbol{\Omega}$ and $\boldsymbol{S}$ are the vorticity tensor and rate of strain tensor, respectively. The peak value of $Q$ was used to identify the center of the vortex and set as the origin for the contour slices. In addition to the Q-criterion, the tangential velocity distribution downstream of the canard was computed to quantify the induced velocity due to the tip vortex. The tangential velocity was computed by converting the cross-stream velocity components into polar coordinates. The tangential velocity, $V_\theta$, is expressed in Eq. 7.

$$V_\theta = V\cos(\theta) - W\sin(\theta), \tag{7}$$

where $V$ and $W$ are the cross-stream and normal velocity components, respectively, and $\theta$ is the rotation angle about the center of the vortex.

Figure 16 presents the nondimensional vorticity, Q-criterion, and tangential velocity for all oscillation amplitudes at x/c = 2 downstream of the canard tip at a reduced frequency of $k_2 = 1$ and at $M_\infty = 0.5$. As was found in Fig. 12, the tip vortex from the baseline case results in a coherent structure indicated by a high concentration of vorticity near the center of the vortex (Fig. 16a). The Q-criterion value shows the isolated regions of rotation similar to the vorticity field (Fig. 16d). The tangential velocity contour shows a typical vortex-structure concentration of high velocity symmetric about the center of the vortex, which defines the vortex core radius and low velocity within the core. Outside the core, the velocity reduces asymptotically in the radial direction (Fig. 16g). The effect of actuation is noticeable for both A = 1.5° and A = 5° oscillations (Figs. 16b, 16e, 16h, and 16c, 16f, and 16i, respectively). The vorticity field shows a reduction in magnitude stretched in the normal direction compared with the baseline case (Fig. 16b and c). Moreover, the larger amplitude case shows 2 concentrations of vorticity approximately symmetric about the cross-stream direction. The Q-criterion shows a considerable reduction in magnitude and is skewed in the normal direction (Figs. 16e and 16f). The tangential velocity show that actuation causes the vortex

to become distorted, depicted by the asymmetric concentrations of velocity about the vortex core (Fig. 16h). The results indicate an increase in the radius of the vortex core. Furthermore, the wake flow structure for the larger amplitude case is no longer a coherent vortex (Fig. 16i). Interestingly, although the vorticity and tangential velocity magnitude are considerably less than the baseline for both actuated combinations, there is greater influence of tangential velocity in the radial direction (Figs. 16h and 16i). The results prove that the tip vortex obeys conservation of angular momentum.
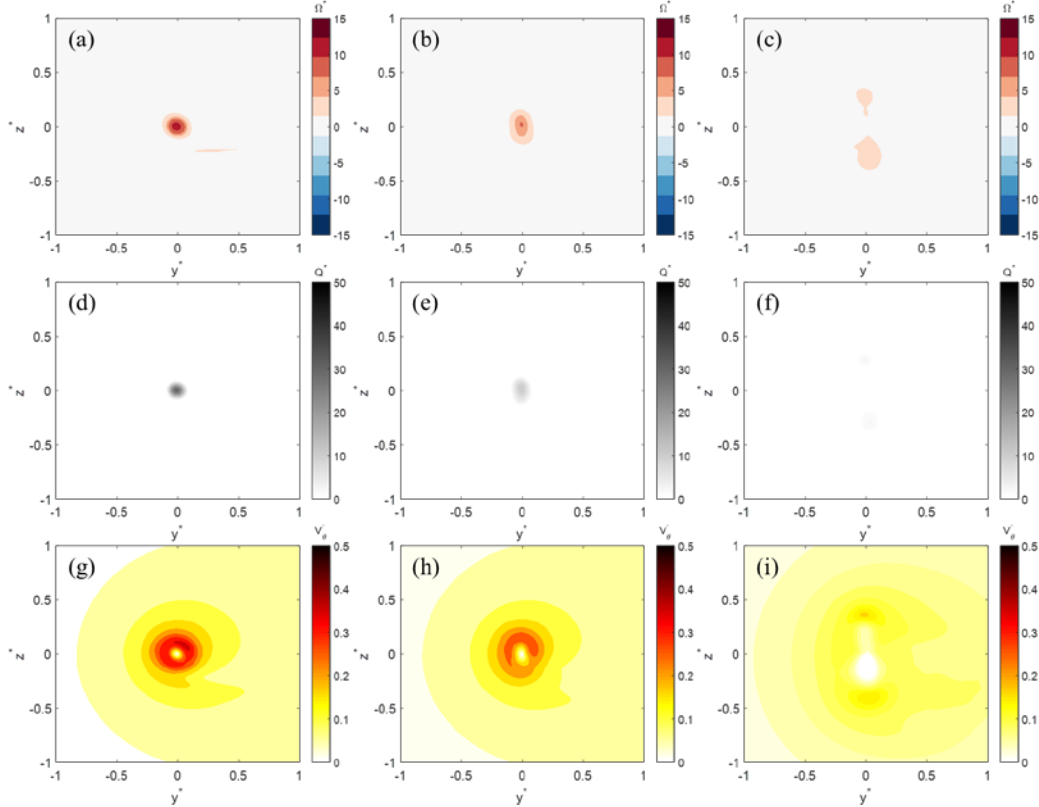


**Fig. 16    Contours of time-averaged nondimensional vorticity (a–c), q-criterion (d–f), and tangential velocity (g–i) at x/c = 2 downstream of canard tip for baseline (a, d, and g), a = 1.5° (b, e, and h), and a = 5° (c, f, and i) case at reduced frequency, $k_2$ = 1.0, $M_\infty$ = 0.5**

Expanding the analysis to all downstream locations, distributions of vorticity magnitude and tangential velocity for all parameter combinations are presented in Figs. 17 and 18, respectively. The distributions are presented at each downstream location along the centerline in both spanwise (z*, represented by solid lines) and cross-stream (y*, represented by dashed lines) directions of the cut plane between z* and y* = –1 to 1. The vorticity distribution defines the profile of vorticity concentration normal to the cut plane, typically exhibiting a peak at the center of the vortex while decreasing asymptotically in the radial direction. Furthermore, the

tangential velocity distributions show a linear region near the center, radially increasing until achieving a maximum at the edge of the vortex, defining the core radius, and then asymptotically decreases.
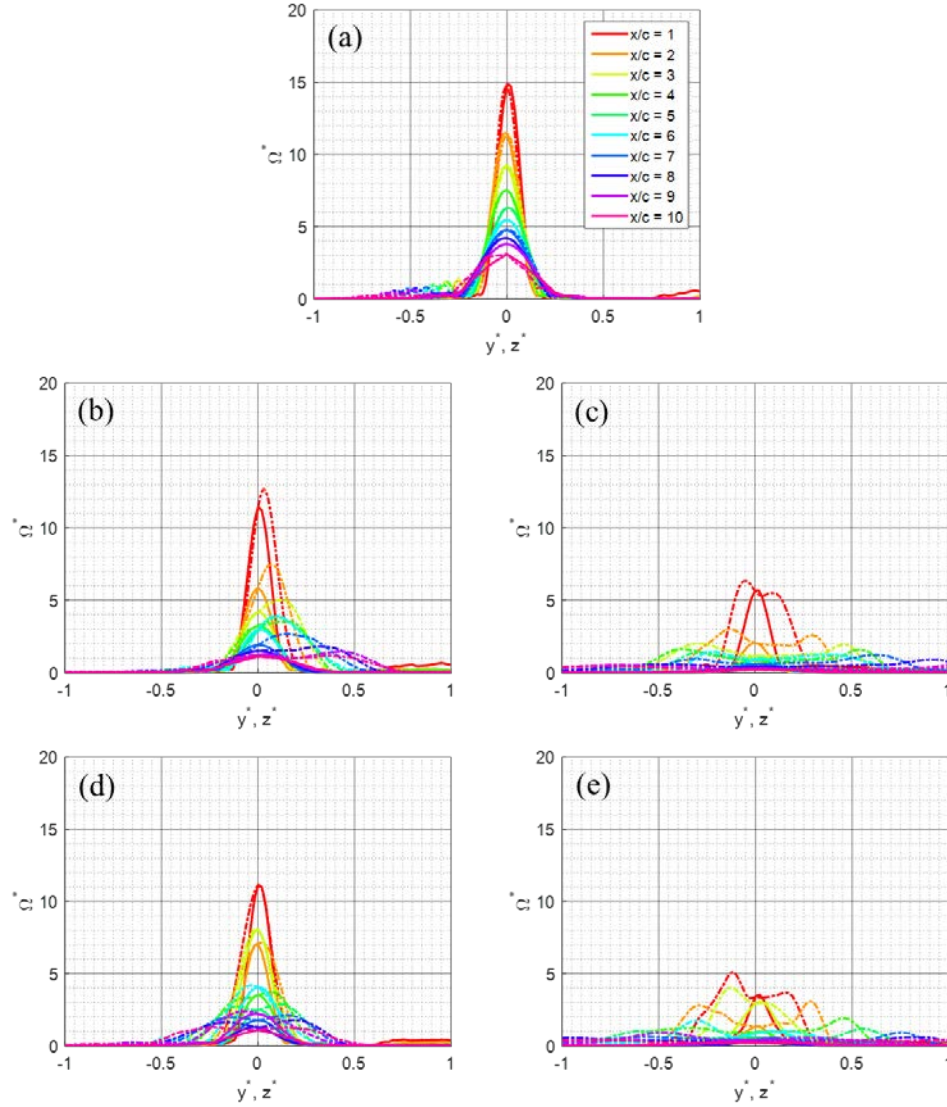


**Fig. 17 Distributions of time-averaged nondimensional vorticity magnitude along centerline in both spanwise ($z^*$, solid) and cross-stream ($y^*$, dashed) directions at $x/c = 1$ to 10 downstream of canard tip for baseline (a), $a = 1.5°$ (b, d) and $5.0°$ (c, e), at reduced frequencies, $k_2 = 0.5$ (b–c) and 1.0 (d–e), at $M_\infty = 0.5$**
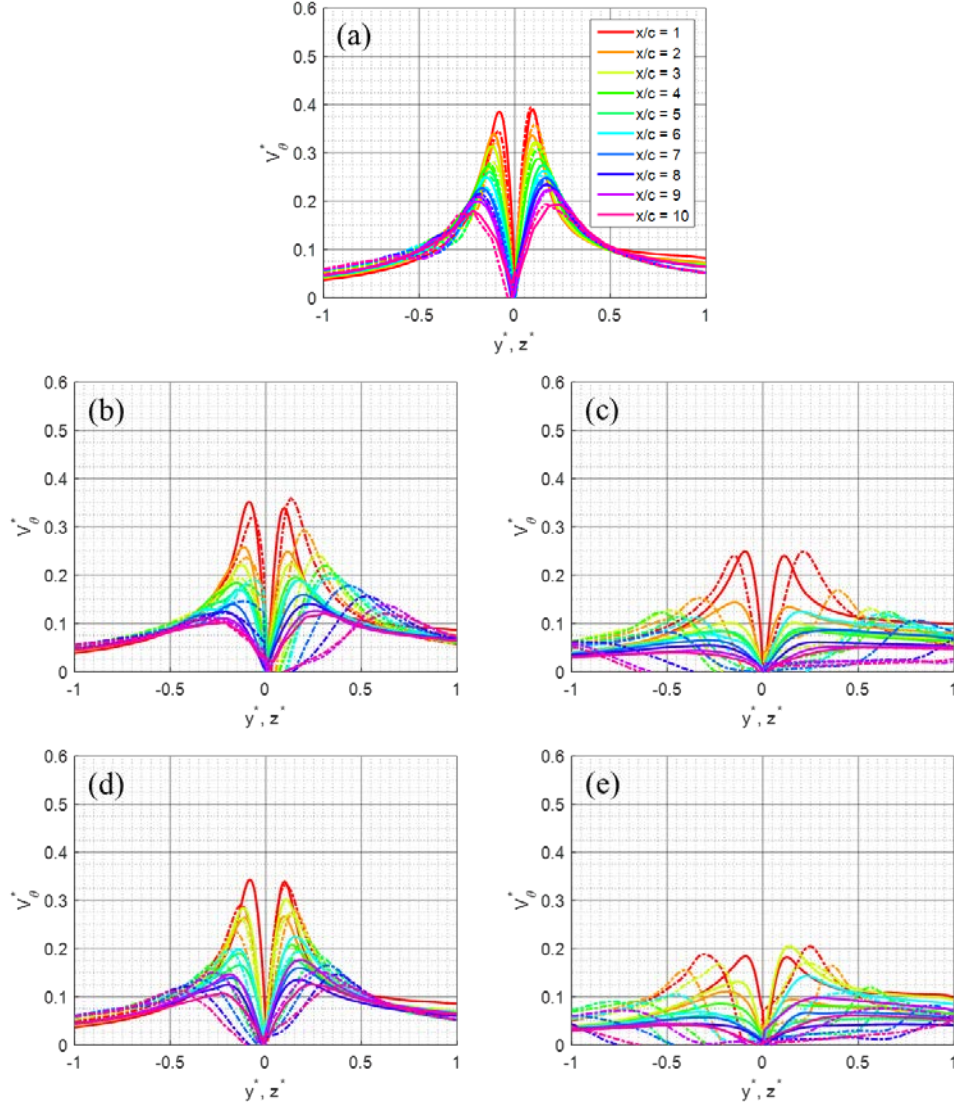
**Fig. 18    Distributions of time-averaged nondimensional tangential velocity along centerline in both spanwise (z\*, solid) and cross-stream (y\*, dashed) directions at x/c = 1 to 10 downstream of canard tip for baseline (a), a = 1.5° (b, d) and 5.0° (c, e), at reduced frequencies, $k_2 = 0.5$ (b–c) and 1.0 (d–e), at $M_\infty = 0.5$**

The baseline distributions of both the vorticity magnitude and tangential velocity show symmetry in both cross and spanwise directions (Figs. 17a and 18a). As expected, the peak vorticity values are within the vortex core, whereas the tangential vorticity reaches a maximum at the edges of the vortex core. Furthermore, the magnitude of vorticity and tangential velocity is inversely proportional to downstream distance, x/c. Compared with the baseline, all actuated combinations show significant decreases in magnitude for both vorticity and tangential velocity at each given downstream location (Fig. 17b–d). Moreover, as the vorticity peak drops, the radial influence increases, obeying conservation of

angular momentum. In actuated cases, both vorticity magnitude and tangential velocity distributions show asymmetry along each cross-stream direction as well as along the streamwise direction at different downstream locations, suggesting that the vortex core moves as the vortex advects downstream (Figs. 17b–d and Figs. 18b–d).

Increasing the amplitude of pitch-oscillation causes a greater reduction in magnitude and increase in radial influence for both vorticity and tangential velocity (Figs. 17c and 17e, and Figs. 18c and 18e). The distributions of tangential velocity show that the larger amplitude oscillation case significantly disrupted the development of the tip vortex, resulting in negligible values of tangential velocity past $x/c = 7$ downstream of the canard tip (Figs. 18c and 18e). The effect-reduced frequency is not as noticeable as amplitude; however, the peak values of vorticity magnitude and tangential velocity downstream are dependent on the wave length of the standing wave wake flow, as similarly shown in Fig. 12. To clearly quantify the effect of the multiple actuation combinations on the development of the tip vortex, the peak values of the parameters to characterize a vortex, as identified previously, was explored.

Figure 19 presents the time-averaged nondimensional peak values of vorticity magnitude, Q-criterion, circulation, tangential velocity, and vortex core radius at 10 downstream locations from the canard tip. Figure 19 identifies the peak values and circulation within the area $y^* = -1$ to 1, $z^* = -1$ to 1 about the vortex center at each downstream location. The strength of a vortex can be characterized through circulation, or the flux of vorticity. The maximum vortex core radius is defined as the distance from the center of the vortex to the radial location of peak tangential velocity.
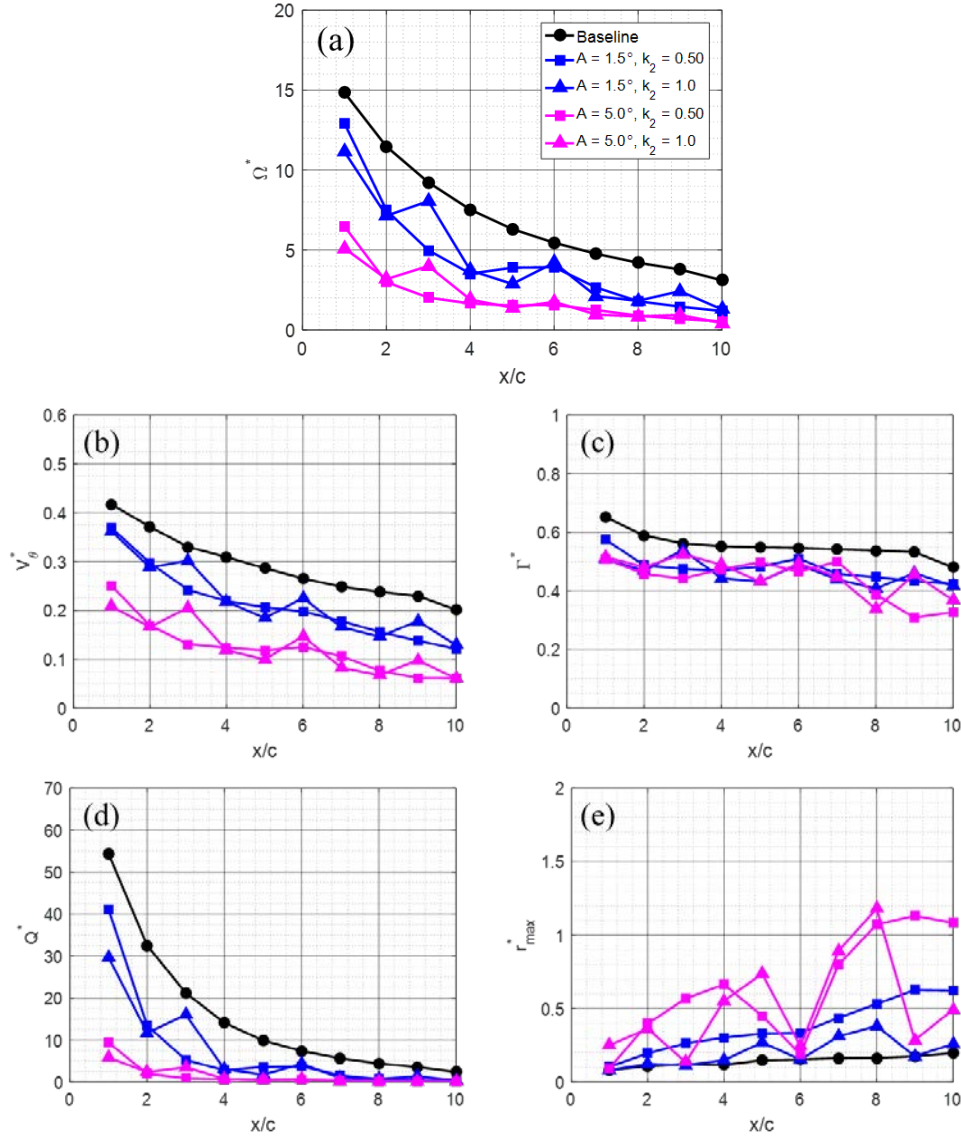
**Fig. 19**   **Line plots of time-averaged nondimensional peak vorticity (a), tangential velocity (b), circulation (c), Q-criterion (d), and vortex core radius (e) at x/c = 1 to 10 downstream of canard tip for baseline, A = 1.5° , and A = 5° cases at reduced frequencies, $k_2$ = 0.5 and 1.0, at $M_\infty$ = 0.5**

For all cases, the peak vorticity value is inversely proportional to downstream location (Fig. 19a). The vorticity decays due to viscosity. Compared with the baseline, pitch oscillating the canard causes the peak vorticity value to significantly decrease at all downstream locations. The increase in amplitude of the oscillation is more effective in reducing the peak vorticity than actuation frequency. The effect of frequency can be seen through the shape of the vorticity distribution: the vorticity peaks define the nodes of the standing wave as similarly observed in Fig. 12. Similar behavior is observed for Q-criterion (Fig. 19d). The effect of actuation significantly reduces the peak Q-criterion values when compared with the

25

baseline case. The results suggest that the development of the tip vortex has been altered due to actuation and that the rotational components of the vortex have been significantly reduced. Furthermore, the peak tangential velocity distribution shows a decrease in magnitude with actuation (Fig. 19b). The tip vortex follows the conservation of angular momentum, and therefore the decrease in vorticity results in an increase of the vortex core radius (Fig. 19e). The decrease in vorticity magnitude results in a greater radial influence of tangential velocity. The circulation distribution supports these findings, as the flux of vorticity is conserved for all combinations (Fig. 19c).

Further research is required to understand which parameter (tangential velocity, vorticity, etc.) produces detrimental performance during vortex–fin interactions. Although the pitch oscillation motion was able to reduce the vorticity of the tip vortex, the result led to a radial increase of tangential velocity. It is possible that the increased area of influence will cause further performance detriment in vortex–fin interactions. Future work is planned to investigate the performance of a downstream control surface in the wake of a pitch-oscillating canard.

## 4.   Conclusion

Lift enhancement was observed for a 2-D airfoil and a 3-D canard undergoing ramp pitch oscillation at high frequency and amplitude. The actuated cases were able to generate higher lift coefficients at higher angles of attack, demonstrating successful implementation of dynamic stall. Although lift augmentation was observed, achieving the necessary amplitude of oscillation for such an effect could prove to be impractical. Furthermore, the dynamic effect was negligible at low angles of attack. In addition to lift enhancement, the effect of pitch oscillation was studied as a possible way to mitigate the tip vortex. The time-averaged flow solution of the actuated cases demonstrated a decrease in vorticity magnitude, TKE, Q-criteria, and tangential velocity. However, the radial influence of the vortex was increased due conservation of angular momentum. Additional work investigating the effect of the altered vortex on the performance of a control surface farther downstream is required and will be pursued.

## 5.   References

1.   Fresconi F, Brown G, Celmins I, DeSpirito J, Ilg M, Maley J, Magnotti P, Scanlan A, Stout C, Vazquez E. Very affordable precision projectile technology development and flight demonstrations. Aberdeen Proving Ground (MD): Army Research Laboratory (US); 2011 Mar. Report No.: ARL-TR-5460.

2.   Fresconi FE, Harkins T. Experimental flight characterization of asymmetric and maneuvering projectiles from elevated gun firings. Journal of Spacecraft and Rockets. 2012;49(6):1120–1130.

3.   Celmins I, inventor. Method and apparatus for correcting the trajectory of a fin-stabilized, ballistic projectile. The United States of America as Represented by the Secretary of the Army, assignee. United States patent US 8,933,383, 2015 Jan 13.

4.   Fresconi FE, Celmins I, Silton S, Costello M. High maneuverability projectile flight using low cost components. Aerospace Science and Technology. 2015;41:175–188.

5.   Fresconi F, Celmins I, Ilg M, Maley J. Projectile roll dynamics and control with a low-cost skid-to-turn maneuver system. Journal of Spacecraft and Rockets. 2014;51(2):624–627.

6.   Silton SI, Fresconi FE. High maneuverability airframe: initial investigation of configuration AFT end for increased stability, range, and maneuverability. Aberdeen Proving Ground (MD): Army Research Laboratory (US); 2013 Sep. Report No.: ARL-TR-6585.

7.   DeSpirito J, Vaughn ME, Washington WD. Numerical investigation of aerodynamics of canard-controlled missile using planar and grid tail fins. Part 1. supersonic flow. Aberdeen Proving Ground (MD): Army Research Laboratory (US); 2002 Oct. Report No.: ARL-TR-2848.

8.   DeSpirito J, Vaughn ME, Washington WD. Numerical investigation of aerodynamics of canard-controlled missile using planar and grid tail fins. Part II. subsonic and transonic flow. Aberdeen Proving Ground (MD): Army Research Laboratory (US); 2004 Mar. Report No.: ARL-TR-3162.

9.   Washington WD, Miller M. Grid fins – a new concept for missile stability and control. Proceedings of the 31st Aerospace Sciences Meeting. Reston (VA): American Institute of Aeronautics and Astronautics; 1993. AIAA Paper No.: 93-0035.

10. Silton SI, Coyle CJ. Effect of canard deflection for roll control on fin performance of a fin-stabilized projectile. Proceedings of the 54th AIAA Aerospace Sciences Meeting. Reston (VA): American Institute of Aeronautics and Astronautics; 2016. AIAA Paper No.: 2016-0309.

11. Silton SI. Effect of canard deflection for pitch and yaw on fin performance of a fin-stabilized projectile. Proceedings of the 33rd AIAA Applied Aerodynamics Conference. Reston (VA): American Institute of Aeronautics and Astronautics; 2015. AIAA Paper No.: 2015-2586.

12. Silton SI, Fresconi FE. The effect of canard interactions on aerodynamic performance of a fin-stabilized projectile. Proceedings of the 53rd AIAA Aerospace Sciences Meeting. Reston (VA): American Institute of Aeronautics and Astronautics; 2015. AIAA Paper No.: 2015-1924.

13. Blair AB. Wind tunnel investigation at supersonic speeds of a canard controlled missile with fixed and free-rolling tail fins. Washington (DC): National Air and Space Administration; 1978. NASA Technical Paper No.: 1316.

14. Blair AB, Allen JM, Hernandez G. Effect of tail fin span on stability and control characteristics of a canard-controlled missile at supersonic Mach numbers. Washington (DC): National Air and Space Administration; 1983. NASA Technical Paper No.: 2157.

15. Smith EH, Hebbar SK, Platzer MF. Aerodynamic characteristics of a canard-controlled missile at high angles of attack. Journal of Spacecraft and Rockets, 1994;31(5):766–772.

16. Meyer J. Effects of the roll angle on cruciform wing-body configurations at high incidences. Journal of Spacecraft and Rockets. 1994;31(1):113–122.

17. Auman LM, Kreeger RE. Aerodynamic characteristics of a canard controlled missile with a free-spinning tail. Proceedings of the 36th AIAA Aerospace Sciences Meeting and Exhibit. Reston (VA): American Institute of Aeronautics and Astronautics; 1998. AIAA Paper No.: 1998-0410.

18. McDaniel MA, Evans C, Lesieutre DJ. The effect of tail fin parameters on the induced roll of a canard-controlled missile. Proceedings of the 28th AIAA Applied Aerodynamics Conference. Reston (VA): American Institute of Aeronautics and Astronautics; 2010. AIAA Paper No.: 2010-4226.

19. Lesieutre DJ, Quijano O. Studies of vortex interference associated with missile configurations. Proceedings of the 52nd Aerospace Sciences Meeting. Reston (VA): American Institute of Aeronautics and Astronautics; 2015. AIAA Paper No.: 2015-0213.

20. Gülçat Ü. Fundamentals of modern unsteady aerodynamics. Heidelberg (Germany): Springer-Verlag; 2010.

21. McCroskey WJ. Unsteady airfoils. Annual Review of Fluid Mechanics. 1982;14(1):285–311.

22. Harper PW, Flanigan RE. The effect of rate of change of angle of attack on the maximum lift of a small model. Washington (DC): National Advisory Committee for Aeronautics; 1950. NACA Technical Note No.: 2061.

23. Calderon DE, Wang Z, Gursul I. Lift enhancement of a rectangular wing undergoing a small amplitude plunging motion. Proceedings of the 48th Aerospace Sciences Meeting. Reston (VA): American Institute of Aeronautics and Astronautics; 2010. AIAA Paper No.: 2010-386.

24. Cleaver DJ, Wang ZJ, Gursul I. Delay of stall by small amplitude airfoil oscillation at low Reynolds numbers. Proceedings of the 47th Aerospace Sciences Meeting. Reston (VA): American Institute of Aeronautics and Astronautics; 2009. AIAA Report No.: 2009-392.

25. Cleaver DJ, Wang ZJ, Gursul I, Visbal MR. Lift enhancement by means of small amplitude airfoil oscillations at low Reynolds numbers. AIAA Journal. 2011;49(9):2018–2033.

26. Cleaver DJ, Wang ZJ, Gursul. Lift enhancement on oscillating airfoils. Proceedings of the 39th Fluid Dynamics Conference. Reston (VA): American Institute of Aeronautics and Astronautics; 2009. AIAA Paper No.: 2009-4028.

27. Baik YS, Bernal LP, Shyy W, Ol MV. Unsteady force generation and vortex dynamics of pitching and plunging flat plates at low Reynolds number. Proceedings of the 49th Aerospace Sciences Meeting; 2011. AIAA Paper No.: 2011-220.

28. Anderson JM, Streitlien K, Barret DS, Triantafyllou MS. Oscillating foils of high propulsive efficiency. Journal of Fluid Mechanics. 1998;360:41–72.

29. Piziali RA. 2-D and 3-D oscillating wing aerodynamics for a range of angle of attack including stall. Washington (DC): National Air and Space Administration; 1993. NASA Technical Memorandum No.: 4632.

30. McCroskey WJ. The phenomenon of dynamic stall. Washington (DC): National Air and Space Administration; 1981. NASA Technical Paper No.: 81264.

31. Corke TC, Thomas FO. Dynamic stall in pitching airfoils: aerodynamic damping and compressibility effects. Annual Review of Fluid Mechanics. 2015;47:479–505.

32. McAlister KW, Carr LW, McCroskey WJ. Dynamic stall experiments on the NACA 0012 airfoil. Washington (DC): National Air and Space Administration; 1978. NASA Technical Paper No.: 1100.

33. Carr LW, McAlister KW, McCroskey WJ. Analysis of the development of dynamic stall based on oscillating airfoil experiments. Washington (DC): National Air and Space Administration; 1977. NASA Technical Note No.: D-8382.

34. Koochesfahani MM. Vortical patterns in the wake of an oscillating airfoil. Proceedings of the 25th Aerospace Sciences Meeting. Reston (VA): American Institute of Aeronautics and Astronautics; 1987. AIAA Paper No.: 87-0111.

35. Jones KD, Dohring CM, Platzer MF. Wake structures behind plunging airfoils: a comparison of numerical and experimental results. Proceedings of the 34th Aerospace Sciences Meeting. Reston (VA): American Institute of Aeronautics and Astronautics; 1996. AIAA Paper No.: 96-0078.

36. Koochesfahani MM, Bohl DG. MTV measurements of the vertical field in the wake of an airfoil oscillating at high reduced frequency. Journal of Fluid Mechanics. 2009;620:63–88.

37. Liiva J. Unsteady aerodynamic and stall effects on helicopter rotor blade airfoil sections. Journal of Aircraft. 1963;6(1):46–51.

38. McCroskey WJ. Vortex wakes of rotorcraft. Proceedings of the 33rd Aerospace Sciences Meeting. Reston (VA): American Institute of Aeronautics and Astronautics; 1995. AIAA Paper No.: 95-0530.

39. Caradonna FX, Laub GH, Tung C. An experimental investigation of the parallel blade-vortex interaction. Washington (DC): National Air and Space Administration: 1984. NASA Technical Memorandum No.: 86005.

40. Rockwell D. Vortex-body interactions. Annual Review of Fluid Mechanics. 1998;30:199–229.

41. Metacomp Technologies, Inc. MIME user manual. Agoura Hills (CA): Metacomp; 2010.

42. Metacomp Technologies, Inc. CFD++ user manual, Agoura Hills (CA): Metacomp; 2011.

43. Jeong J, Hussain F. On the identification of a vortex. Journal of Fluid Mechanics. 1995;285:69–94.

44. Hunt JCR, Wray AA, Moin P. Eddies, streams, and convergence zones in turbulent flows. Stanford (CA): Center for Turbulence Research (CTR); 1988. CTR Report No.: S88. p. 193.

45. Haller G. An objective definition of a vortex. Journal of Fluid Mechanics. 2005;525:1–26.

46. Green MA, Rowley CW, Haller G. Detection of Lagrangian coherent structures in 3-D turbulence. Journal of Fluid Mechanics. 2007;575:111–120.

47. Kolář V. Vortex identification: new requirements and limitations. International Journal of Heat and Fluid Flow. 2007;28:638–652.

## List of Symbols, Abbreviations, and Acronyms

| | |
|---|---|
| 2-D | 2-dimensional |
| 3-D | 3-dimensional |
| ARL | US Army Research Laboratory |
| CFD | computational fluid dynamics |
| CFL | Courant-Friedrichs-Lewy |
| DSRC | Department of Defense Supercomputing Resource Center |
| NACA | National Advisory Committee for Aeronautics (NACA) |
| RANS | Reynolds-averaged Navier-Stokes |
| TKE | turbulent kinetic energy |

| | | |
|---|---|---|
| 1 (PDF) | DEFENSE TECHNICAL INFORMATION CTR DTIC OCA | RDRL WML C S AUBERT |
| 2 (PDF) | DIRECTOR US ARMY RESEARCH LAB RDRL CIO L IMAL HRA MAIL & RECORDS MGMT | RDRL WML D R BEYER RDRL WML E V BHAGWANDIN I CELMINS J DESPIRITO S SILTON F FRESCONI J VASILE P WEINACHT |
| 1 (PDF) | GOVT PRINTG OFC A MALHOTRA | |
| 5 (PDF) | AMRDEC L AUMAN J DOYLE K KENNEDY M MCDANIEL C ROSEMA | RDRL WML F T BROWN M ILG B KLINE J MALEY B NELSON |
| 6 (PDF) | ARDEC M STOLK YIN CHEN T RECCHIA D HOSIER M DUCA G RODEBAUGH | RDRL WML G M MINNICINO J SOUTH RDRL WML H J NEWILL RDRL WMP D LYON RDRL WMM M VANLANDINGHAM |
| 1 (PDF) | NWSCDD G33 S KOSKI | |
| 1 (PDF) | USMA DEPT OF MECHANICAL ENGINEERING C VERHULST | |
| 30 (PDF) | DIR USARL RDRL VTA C KRONINGER RDRL VTV R SINGH RDRL WM B FORCH S KARNA A RAWLETT S SCHOENFELD J ZABINSKI RDRL WML P PEREGINO N TRIVEDI RDRL WML A W OBERLE RDRL WML B E BYRD | |

INTENTIONALLY LEFT BLANK.